The Aeronautical Journal (2026), **130**, pp. 3054–3080
doi:10.1017/aer.2026.10203

RESEARCH ARTICLE

Mass- and momentum-conserved secondary injection model (MMC-SIM) for thrust vector control analysis

Noreen Abdelwahab and Craig Johansen

Department of Mechanical and Manufacturing Engineering, University of Calgary, Calgary, Canada
Corresponding author: Noreen Abdelwahab; Email: noreenabdelwahab@gmail.com

Received: 9 January 2026 UTC; **Revised:** 15 June 2026 UTC; **Accepted:** 16 June 2026 UTC

Keywords: secondary fluid injection; semi-empirical modelling; shock vector control; supersonic nozzle; thrust vectoring

Abstract

A mass- and momentum-conserved secondary injection model (MMC-SIM) is presented for thrust vector control (TVC) analysis in axisymmetric nozzles. TVC modelling provides fast thrust vector predictions for control design, preliminary nozzle sizing, and integration into flight simulation frameworks. Existing low-order models rely on simplifying assumptions regarding the secondary jet exit state, which limits reproducibility and can compromise predictive accuracy. MMC-SIM addresses this limitation by reformulating the equivalent obstruction height problem. Mass conservation and momentum conservation provide two independent constraints that are solved simultaneously to determine both the effective injection height and the secondary jet exit state, eliminating the need to prescribe downstream jet conditions a priori. These constraints are embedded within a blunt-body framework to predict boundary layer separation, wall pressure distribution and thrust vector characteristics. Computational fluid dynamics (CFD) simulations are used to assess the modelling assumptions and examine the flow structures. MMC-SIM shows strong agreement with experimental results, yielding average and maximum lateral force prediction errors of 3.3% and 4.8%, respectively. Compared to current leading models, MMC-SIM substantially improves the prediction of the pressure-driven lateral force while providing a transparent and reproducible modelling framework suitable for engineering design applications.

Nomenclature

A	cross-sectional area
$C_{P\max}$	maximum pressure coefficient
D_{inj}	diameter of secondary injection port
F_{j}	force due to secondary jet momentum
F_y	total lateral thrust
F_{net}	net externally applied forces on control volume
F_P	force due to wall pressure
h	characteristic height of secondary injection
M	Mach number
$\dot{m}$	mass flow rate
n	surface normal unit vector
P	pressure
P_b	back-pressure acting on control volume exit face
P_f	pressure on forward-facing step face
q	dynamic pressure
R	specific gas constant
R_C	shock hyperbola vertex radius of curvature
R_s	separation hyperbola vertex radius of curvature
r	radius

© The Author(s), 2026. Published by Cambridge University Press on behalf of Royal Aeronautical Society. This is an Open Access article, distributed under the terms of the Creative Commons Attribution licence (https://creativecommons.org/licenses/by/4.0/), which permits unrestricted re-use, distribution and reproduction, provided the original article is properly cited.
https://doi.org/10.1017/aer.2026.10203 Published online by Cambridge University Press

T	temperature
U	velocity vector
X_s	boundary layer separation distance
x	longitudinal axis, aligned with the rocket axis
α_n	conical nozzle half-angle
β'	proportionality constant set to 0.062
γ	ratio of specific heats
Δ	bow shock standoff distance
δ	flow deflection angle for oblique shock wave
ζ	oblique shock wave angle
Θ	obstruction local inclination angle
θ	Mach angle/hyperbola asymptote angle
ρ	density
Ψ	rotation angle

Subscripts and superscripts

amb	ambient conditions
e	exit
in	secondary jet conditions at injection port
inj	secondary injection
plat	plateau region
s	condition at boundary layer separation location
t	stagnation state
$*$	sonic state

1.0 Introduction

The growing demand to launch payloads into orbit has accelerated the development of high-performance rockets [1, 2]. Modern rockets require enhanced manoeuvrability to perform trajectory corrections, docking, deorbiting, reentry and landing [3]. Requiring high control authority, thrust vector control (TVC) is used to maintain vehicle flight stability and desired trajectory [4]. One method for manipulating thrust direction involves injecting fluid laterally into the nozzle in a method known as secondary injection thrust vector control (SITVC) [5, 6]. SITVC has advantages over conventional TVC mechanisms. It eliminates moving mechanical components associated with movable nozzles and generates higher lateral thrust when compared to cold gas thrusters in vacuum [7]. Additionally, SITVC is particularly relevant for hybrid rocket technologies, as the liquid oxidiser may be used for injection, eliminating challenging flex-seal nozzles [8]. Furthermore, it is effective across a wide range of flight regimes, including both atmospheric and vacuum conditions [3]. Lastly, active flow control via secondary injection shows great potential for use on dual-bell nozzles [9].

Despite these advantages, accurate prediction of thrust vector generation in SITVC nozzles remains challenging. The injected jet interacts strongly with the supersonic primary flow, producing oblique shocks, bow shocks, boundary layer separation, turbulent vortical structures and highly asymmetric wall pressure distributions that collectively determine the resulting thrust vector. High-fidelity numerical simulations and experiments can resolve these complex interactions, but their computational and experimental cost makes them impractical for rapid design iteration, parametric studies or real-time simulation environments. Reduced-order models therefore remain important engineering tools, offering speed and affordability over experimental and computational techniques. They are also particularly suitable for integration into six degree-of-freedom rocket simulation frameworks.

Early SITVC models largely relied on empirical correlations, correction factors and experimental calibration [10–16]. Rather than serving as standalone predictive frameworks that directly map injectant properties and nozzle geometry to thrust vector outputs, these models required extensive experimental

https://doi.org/10.1017/aer.2026.10203 Published online by Cambridge University Press

calibration. Moreover, this calibration depended heavily on the specific compositions of both the injectant and the primary rocket motor thrust, leading to models that are not readily generalisable to new propellant-injectant combinations and hindering the reproducibility of results.

Subsequent semi-empirical blunt-body models reduced the dependence on injectant- and propellant-dependent calibration factors, leading to improved generalisability and establishing standalone SITVC prediction frameworks [17–20]. By treating the injected secondary jet as an equivalent physical obstruction to the primary supersonic flow, these models could estimate key flow characteristics including boundary layer separation, wall pressure distributions and resultant thrust. However, a critical limitation persisted: the conditions of the secondary jet at the nozzle exit remained unknown, yet were required for determining the effective obstruction geometry. To circumvent this, these frameworks commonly prescribe arbitrary secondary jet exit conditions, or introduce auxiliary assumptions regarding jet behaviour downstream of injection. Such assumptions can introduce substantial deviations from conservation principles, reduce reproducibility and obscure the physical basis of model predictions.

This work develops a new semi-empirical framework for SITVC analysis, termed the mass- and momentum-conserved secondary injection model (MMC-SIM), that removes this closure deficiency. Rather than prescribing the downstream jet state, MMC-SIM determines the equivalent obstruction geometry by simultaneously satisfying mass and momentum conservation constraints on a control volume surrounding the injected jet. This coupled conservation closure yields both the effective injection height and the secondary jet exit condition as part of the solution, providing a physically constrained and transparent analytical framework for thrust vector prediction.

The contributions of this work are as follows:

1. A coupled mass-momentum closure formulation is developed for determining the effective obstruction geometry in blunt-body SITVC modelling.
2. A fully specified and reproducible implementation is presented, including explicitly solution procedures and governing relations.
3. The framework predicts intermediate flow quantities (including separation location and wall pressure distribution) in addition to overall thrust vector characteristics.
4. Computational fluid dynamics (CFD) simulations are used to examine dominant flow structures and assess assumptions underlying the MMC-SIM formulation, while model validation is performed against experimental measurements reported in the literature.

The remainder of this paper first reviews existing modelling approaches for SITVC, then presents the MMC-SIM formulation, followed by a limited CFD-based flow analysis used to examine dominant interaction structures and evaluate key modelling assumptions, before validation against available experimental data.

2.0 Background on modelling of SITVC

Secondary injection thrust vector control generates lateral force through coupled momentum addition and pressure-induced loading on the nozzle wall. Figure 1 schematically illustrates the key flow phenomena responsible for lateral thrust generation in an SITVC nozzle and is adapted from Fig. 1 in Ref. (21). Following injection, the secondary jet interacts strongly with the supersonic primary flow, producing an upstream separation shock, a bow shock enveloping the injected jet, boundary layer separation and a highly asymmetric wall pressure distribution. In addition to direct momentum injection by the secondary jet, this pressure asymmetry contributes substantially to lateral force generation and overall thrust vectoring performance.

The complex three-dimensional flow involves shock-wave/boundary-layer interaction, turbulent mixing, jet expansion and recirculation regions [22, 23]. Accurate first-principles analytical modelling of the full interaction field is therefore intractable. Instead, predictive models simplify the flow physics while retaining the mechanisms most influential to thrust generation.

https://doi.org/10.1017/aer.2026.10203 Published online by Cambridge University Press

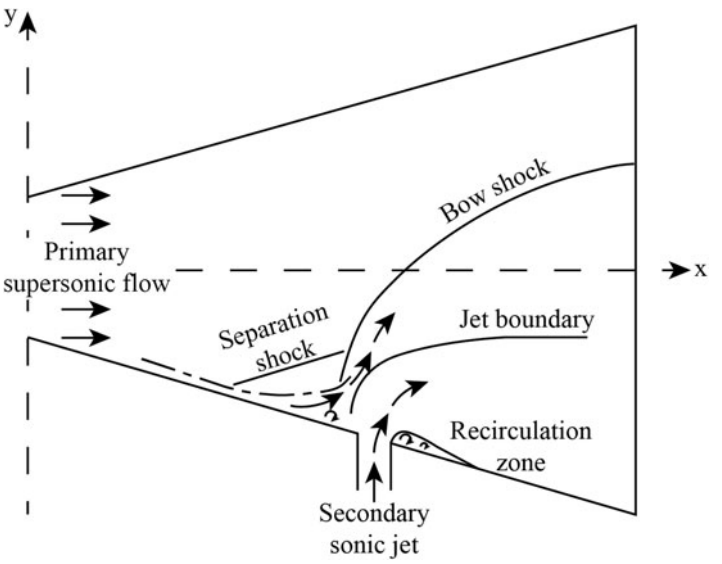


Figure 1. *Schematic of key flow features generated by secondary injection thrust vector control.*

Most analytical SITVC models combine theoretical analysis with empirical correlations to estimate these quantities [4, 14]. Their differences primarily lie in how the equivalent obstruction is defined, how wall pressure distributions are represented and how the secondary jet state is modelled. These distinctions give rise to several broad classes of analytical models, reviewed in the following section.

A central unresolved challenge across reduced-order SITVC modelling is the closure of the secondary jet interaction problem. The effective obstruction geometry and downstream jet state are not directly known, yet both strongly influence predicted separation behaviour, wall pressure loading and ultimately thrust vector magnitude. Existing approaches typically address this uncertainty through prescribed jet exit conditions or empirical scaling relations. The accuracy and reproducibility of model predictions therefore depend strongly on how this closure problem is treated.

The modelling framework developed in this work focuses specifically on this closure problem. By determining the effective obstruction geometry through simultaneous enforcement of mass and momentum conservation, MMC-SIM replaces prescribed downstream assumptions with a physically constrained closure while retaining the computational efficiency of semi-empirical blunt-body modelling.

Recent advances in computational and experimental investigations have substantially improved the understanding of SITVC flow physics. Modern numerical and experimental studies have investigated parameters affecting thrust vector performance and flow structures within an SITVC nozzle [24–31]. These investigations provide increasingly detailed characterisation of asymmetric pressure loading, shock interaction and vortex dynamics associated with fluidic thrust vectoring. Despite these advances, comparatively few recent developments have focused on reduced-order analytical modelling, where closure of the jet-flow interaction remains a persistent challenge. As a result, analytical and semi-empirical models continue to play an important role in rapid engineering prediction, preliminary design and reduced-order simulation environments.

2.1 Overview of models in the literature

Early analytical modelling efforts established much of the conceptual foundation for SITVC analysis. Wu et al. [15] set an early benchmark by applying conservation of mass, momentum and energy to describe secondary injection interactions. However, the complexity of the jet-freestream interaction required substantial simplifications, limiting the model's ability to accurately predict thrust vector

https://doi.org/10.1017/aer.2026.10203 Published online by Cambridge University Press

behaviour and resolve intermediate flow features such as separation location or wall pressure distribution. Moreover, this framework relied on experimentally derived scaling parameters dependent on the injectant. This dependence means experiments are required for each exhaust-injectant interaction, significantly hindering widespread use of this approach.

Experimental investigations by Zukoski and Spaid [16] later provided important physical insight into the interaction field using Schlieren visualisation. Their observations showed that the injected jet behaves as an effective obstruction to the primary flow, producing a bow shock and upstream flow separation analogous to flow over a blunt body. This led to the development of 'blunt-body' analogies for SITVC modelling, where the secondary jet is represented by an equivalent obstruction in the primary flow. Prediction of the thrust generated in an SITVC nozzle using the blunt-body approach involves three main steps:

1. Determination of an equivalent obstruction, usually using the characteristic height, h
2. Prediction of the resulting wall pressure distribution in the vicinity of the injection port
3. Calculation of the net thrust vector by combining wall pressure and jet momentum contributions

This framework remains attractive because it provides prediction not only of overall thrust, but also of intermediate flow quantities directly linked to vectoring performance.

Subsequent models progressively improved the representation of the wall pressure field. Wilson et al. [14] introduced one of the first semi-empirical formulations that explicitly partitioned the wall pressure distribution into distinct flow regions. Later, Mangin [18] and Maarouf [17] extended the blunt-body approach to axisymmetric nozzles by developing a more complete semi-empirical framework for predicting separation location, pressure loading and thrust vector generation. For brevity, this work refers to this modelling family as the Evry model . Subsequent studies attempted to reproduce the model, but had to introduce additional assumptions and simplifications to address problem closure [24, 32, 33]. More recently, Younes et al. [33] conducted a sensitivity analysis. Of note, they highlight the importance of accurately estimating the shock position and that reliance on empirical relations may introduce additional error.

Despite their usefulness, existing blunt-body formulations share an important modelling limitation: closure of the effective obstruction problem is typically achieved by prescribing unknown downstream jet conditions or by introducing auxiliary assumptions regarding jet geometry or exit behaviour. These quantities are not generally known *a priori*, and as such, the resulting closure can introduce significant deviations from conservation consistency and can make implementation sensitive to modelling assumptions.

This limitation is distinct from the broader use of empirical relations in semi-empirical modelling, which remain valuable for representing difficult-to-model flow phenomena. Rather, the unresolved issue is that the effective obstruction geometry, which fundamentally governs separation distance and wall pressure loading, is often determined through assumed downstream conditions rather than through physically constrained closure.

MMC-SIM builds directly on the blunt-body modelling tradition while addressing this specific limitation. Instead of prescribing the downstream jet state, the equivalent obstruction height is determined as part of the solution through simultaneous satisfaction of mass and momentum conservation constraints. This preserves the interpretability and computational efficiency of reduced-order blunt-body modelling while strengthening its physical consistency and reproducibility.

3.0 Modelling of SITVC

3.1 Overview of MMC-SIM

Building on these foundational works [15, 17, 18, 34, 35], a semi-empirical model was developed to compute the thrust vector for three-dimensional converging-diverging nozzles. The MMC-SIM framework enforces both mass and momentum conservation, avoiding the need for other assumptions seen in subsequent models.

https://doi.org/10.1017/aer.2026.10203 Published online by Cambridge University Press

MMC-SIM predicts the thrust vector in an SITVC nozzle by modelling the secondary jet as an equivalent blunt body with a quarter-sphere nose of radius h, referred to as the injection height. Traditional blunt-body models determine this characteristic dimension, h, by balancing drag against assumed jet exit momentum, which requires prescribing unknown secondary jet exit conditions [16, 17, 32]. MMC-SIM removes this assumption by formulating the equivalent obstruction height as a coupled closure problem: conservation of mass and conservation of momentum provide two independent constraints that are solved simultaneously for both the jet exit state and the corresponding injection height. This enables the determination of the effective obstruction geometry *without prescribing downstream jet conditions a priori.*

3.1.1 Complexity of SITVC flow structures

The three-dimensional flow structure produced by SITVC is inherently complex, involving a horseshoe vortex, a pair of counter-rotating vortices, mixing between the jet and freestream, and recirculation zones. Detailed analytical modelling of these individual phenomena and their interactions is challenging. Instead, the model can be greatly simplified if only the features that contribute significantly to the thrust vector are considered. These features of interest, including the adverse pressure gradient and boundary layer separation, lie near the nozzle wall and may be approximated using a combination of analytical modelling and empirical relations.

3.1.2 Modelling simplifications and assumptions

MMC-SIM applies the blunt-body analogy and the following assumptions for thrust vector predictions:

1. The secondary jet is deflected by the primary freestream until it is parallel to the nozzle wall.
2. The equivalent body has a quarter-sphere nose.
3. No mixing occurs between the primary and secondary flows.
4. Shear stresses on the control volume are negligible.
5. The boundary layer thickness is much less than the injection height.

3.1.3 MMC-SIM architecture

MMC-SIM consists of two subroutines. Using the nozzle geometry and flow properties as inputs, the first subroutine calculates the injection height, h, and the boundary layer separation position, x_s. These intermediate results are passed to the second subroutine, which determines the thrust by numerically integrating the pressure along the nozzle wall. Full details of each subroutine are provided in Sections 3.2 and 3.3. A more detailed implementation of the MMC-SIM algorithm, including full source code and supporting derivations, is provided in the author's thesis [36].

3.2 Subroutine 1: injection height determination

A control volume encompassing the secondary jet is shown in Fig. 2 based on Fig. 6 from Ref. (37). The centre of the secondary injection port is located at x_{inj}. Note that the nozzle divergence (half-angle) is assumed to be small and is neglected. The oncoming primary flow is deflected through the oblique shock upstream of the obstruction by the turning angle, δ. The onset of boundary layer separation occurs at x_s.

The boundary layer separation distance, X_s, which describes the distance from the separation position to the injection port, is defined by assuming that the deflected flow is tangential to the quarter-sphere nose according to Equation (1).

$$X_s \approx h\left(\frac{1}{\sin\delta} - 1\right) \tag{1}$$

https://doi.org/10.1017/aer.2026.10203 Published online by Cambridge University Press

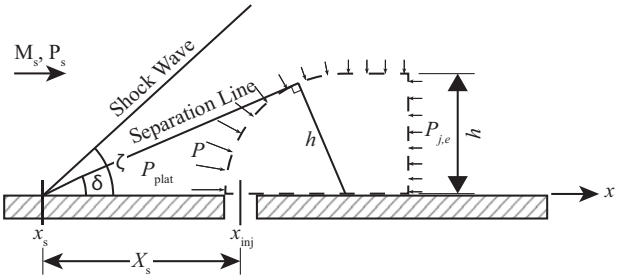


Figure 2. *Control volume encompassing equivalent body with quarter-sphere nose.*

Note that Equation (1) neglects the thickness of the jet. The boundary layer separation position, x_s, is determined using Equation (2).

$$x_s = x_{\text{inj}} - X_s \tag{2}$$

Experimental investigations of supersonic flow over forward-facing steps conducted by Zukoski [35] showed that the pressure within the separated region may be approximated as constant. This so-called plateau pressure, P_{plat}, is primarily dictated by the freestream deflection angle, δ. Jet-induced separation exhibits similar behaviour. However, given that the obstacle size generated by the jet is unknown, empirical relations are used to estimate the plateau pressure from the primary flow properties at x_s. The static pressure of the freestream after the oblique shock, P_{plat} is computed using the empirical relation proposed by Zukoski and given in Equation (3) [35]:

$$P_{\text{plat}} = P_s\,(0.5M_s + 1) \tag{3}$$

Subscript s indicates primary flow properties at the separation position, x_s.

A further increase in pressure occurs immediately upstream of the obstruction. Equation (4) is used to estimate the pressure acting on the upstream face of the obstruction, P_f. The proportionality constant β' was set to 0.062 based on experimental force measurements reported by Zukoski [35] for supersonic transverse injection configurations. Although treating β' as a tunable parameter could potentially improve agreement with numerical simulations or experiments, such an optimisation is beyond the scope of the present work and is left for future investigation. Moreover, the pressure on the upstream face of the control volume does not show dependence on β' if the obstacle height is larger than the boundary layer thickness.

$$P_f = P_{\text{plat}}\left(1 + \beta'\frac{\gamma M_{\text{plat}}^2}{1 + \frac{\gamma-1}{2}M_{\text{plat}}^2}\right) \tag{4}$$

The pressure ratio across the oblique shock, P_{plat}/P_s, is used to find the shock angle, ζ, and the flow deflection angle according to Equations (5) and (6) [38].

$$\sin\zeta = \sqrt{\frac{\frac{P_{\text{plat}}}{P_s}(\gamma+1) + (\gamma-1)}{2\gamma M_s^2}} \tag{5}$$

$$\tan\delta = \cot\zeta\,\frac{M_s^2\sin^2\zeta - 1}{\frac{\gamma+1}{2}M_s^2 - \left(M_s^2\sin^2\zeta - 1\right)} \tag{6}$$

Finally, the Mach number of the freestream flow after the oblique shock is obtained from Equation (7) [38].

$$M_{\text{plat}}^2\sin^2(\delta - \zeta) = \frac{(\gamma-1)\,M_s^2\sin^2\delta + 2}{2\gamma M_s^2\sin^2\delta - (\gamma-1)} \tag{7}$$

https://doi.org/10.1017/aer.2026.10203 Published online by Cambridge University Press

3.2.1 Conservation of mass

The secondary mass flow into the control volume is known and is defined by the secondary injection port flow conditions as follows:

$$\dot{m}_{\text{in}} = \iint \rho U \cdot n dA = \rho_{\text{in}} U_{\text{in}} A_{\text{port}} \tag{8}$$

where the subscript 'in' denotes secondary jet conditions at the injection port with area A_{port}. Assuming that no mixing occurs between the primary and secondary flows, the mass flow rates entering and exiting the control volume are equal by conservation of mass.

$$\dot{m}_{\text{j}} = \dot{m}_{\text{in}} = \dot{m}_{\text{e}} \tag{9}$$

Additionally, the mass flow rate across the exit face is expressed using stagnation properties as follows:

$$\dot{m}_{\text{e}} = \frac{P_{\text{tj}}}{\sqrt{T_{\text{tj}}}} A_{\text{e}} M_{\text{j,e}} \sqrt{\frac{\gamma_{\text{j}}}{R_{\text{j}}}} \left(1 + \frac{\gamma_{\text{j}} - 1}{2} M_{\text{j,e}}^2\right)^{-\frac{\gamma_{\text{j}}+1}{2(\gamma_{\text{j}}-1)}} \tag{10}$$

Subscript 'j' indicates secondary jet properties. Note that the exit area of the control volume is assumed to be a half-circle with radius h.

$$A_{\text{e}} = \frac{\pi}{2} h^2 \tag{11}$$

Rearranging Equation (10) yields an expression for the injection height derived from conservation of mass, as shown in Equation (12).

$$h_{\text{mass}} = \left[\sqrt{\frac{R_{\text{j}}}{\gamma_{\text{j}}}} \frac{2}{M_{\text{j,e}} \pi} \frac{\sqrt{T_{tj}}}{P_{tj}} \dot{m}_{\text{j}} \left(1 + \frac{\gamma_{\text{j}} - 1}{2} M_{\text{j,e}}^2\right)^{\frac{\gamma_{\text{j}}+1}{2(\gamma_{\text{j}}-1)}} \right]^{\frac{1}{2}} \tag{12}$$

Note that the subscript 'mass' indicates that the height is derived from a conservation of mass assumption. Equation (12) establishes the first constraint on the injection height, h. However, the jet exit conditions (specifically Mach number, $M_{\text{j,e}}$) remain unknown. All other parameters in this equation are known.

3.2.2 Conservation of momentum

Applying momentum conservation yields the second constraint on the injection height. The net force in the x-direction, ΣF_x, is balanced by the momentum of the exiting jet, $\dot{m}_{\text{e}} V_{\text{j,e}}$, as established in Equation (13).

$$\sum F_x = F_{x1} + F_{x2} = \dot{m}_{\text{j}} V_{\text{j,e}} \tag{13}$$

Here, F_{x1} and F_{x2} represent the x-components of the forces on the upstream and downstream faces of the control volume, respectively. To evaluate F_{x1}, the pressure on the upstream face of the control volume is integrated.

$$F_{x1} = \iint P \sin\Theta \sin\Phi dA_{\text{upstream}} \tag{14}$$

The differential area over a quarter sphere is illustrated in Fig. 3 (based on Fig. 1.30 in Ref. (39)) and is calculated according to Equation (15). Angles Θ and Φ are defined as illustrated in the figure.

$$dA_{\text{upstream}} = h^2 \sin\Theta d\Theta d\Phi \tag{15}$$

Applying the modified Newtonian theory [40], the pressure on an inclined blunt body is calculated according to Equation (16):

$$P = q_{\text{plat}} C_{P\text{max}} \sin^2\Theta \sin^2\Phi + P_{\text{plat}} \tag{16}$$

https://doi.org/10.1017/aer.2026.10203 Published online by Cambridge University Press

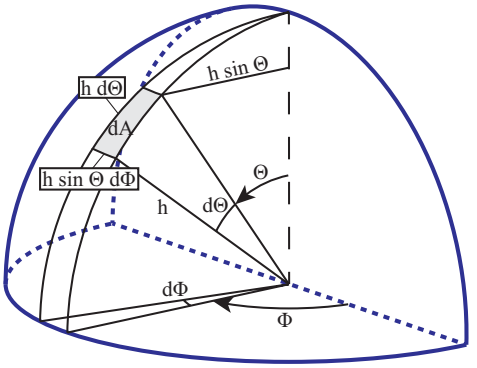


Figure 3. *Schematic of area integration over a quarter sphere.*

Here, $C_{P\max}$ is the maximum pressure coefficient defined according to Modified Newtonian Theory [41]. It is evaluated in the plateau region using Equation (17).

$$C_{P\max} = \frac{2}{\gamma M_{\text{plat}}^2}\left[\frac{\left(\frac{\gamma+1}{2}M_{\text{plat}}^2\right)^{\frac{\gamma}{\gamma-1}}}{\left(\frac{2\gamma}{\gamma+1}M_{\text{plat}}^2-\frac{\gamma-1}{\gamma+1}\right)^{\frac{1}{\gamma-1}}}-1\right] \tag{17}$$

Substituting Equations (15) and (16) into Equation (14) yields the following:

$$F_{x1} = \int_0^{\pi}\int_0^{\pi/2}\left(q_{\text{plat}}C_{P\max}\sin^2\Theta\sin^2\Phi + P_{\text{plat}}\right)h^2\sin^2\Theta\sin\Phi d\Theta d\Phi \tag{18}$$

Evaluating the integral yields Equation (19) for the pressure force on the upstream face of the control volume.

$$F_{x1} = \frac{\pi}{2}h^2\left(\frac{1}{2}q_{\text{plat}}C_{P\max} + P_{\text{plat}}\right) \tag{19}$$

Next, the force acting on the downstream face of the control volume may be determined using Equation (20).

$$F_{x2} = \int PdA = -\frac{\pi}{2}h^2P_b \tag{20}$$

Here, P_b is the back-pressure acting on the downstream control volume face, which equals the undisturbed nozzle exit pressure, P_{e}. Lastly, Equation (21) provides the exiting jet momentum.

$$\dot{m}_{\text{j}}V_{\text{j,e}} = \dot{m}_{\text{j}}M_{\text{j,e}}\sqrt{\gamma_{\text{j}}R_{\text{j}}\frac{T_{\text{tj}}}{1+\frac{\gamma_{\text{j}}-1}{2}M_{\text{j,e}}^2}} \tag{21}$$

Combining Equations (19), (20) and (21) yields a relation for the injection height derived from conservation of momentum:

$$h_{\text{momentum}} = \left[\frac{2}{\pi}\frac{\dot{m}_{\text{j}}M_{\text{j,e}}\sqrt{\gamma_{\text{j}}R_{\text{j}}T_{\text{j,e}}}}{\frac{1}{2}q_{\text{plat}}C_{P\max}+P_{\text{plat}}-P_{\text{b}}}\right]^{1/2} \tag{22}$$

Note that the subscript 'momentum' indicates that the height is derived from a conservation of momentum assumption. As in the equation derived from continuity, the jet exit condition remains unknown ($M_{\text{j,e}}$, $T_{\text{j,e}}$). All other parameters in Equation (22) are known.

https://doi.org/10.1017/aer.2026.10203 Published online by Cambridge University Press

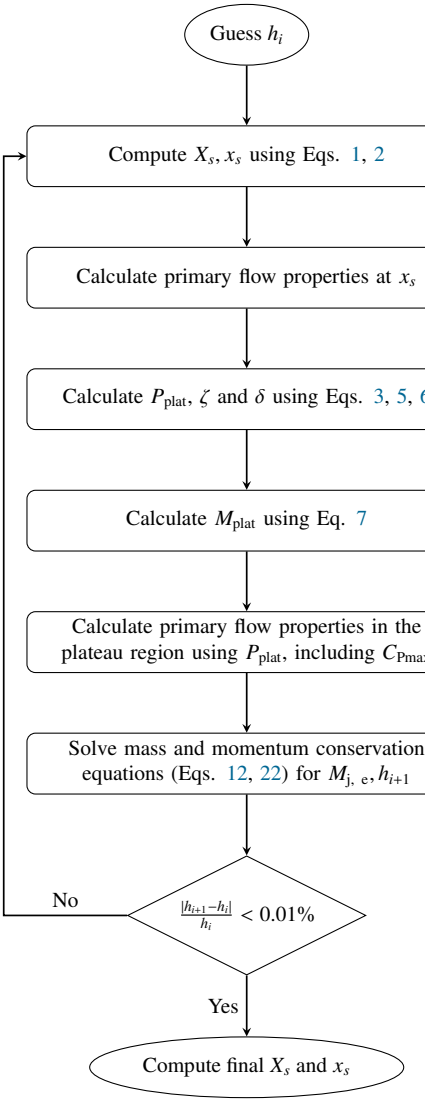


Figure 4. *Numerical implementation workflow for coupled conservation closure in MMC-SIM.*

3.2.3 Numerical implementation of the coupled solution procedure

Figure 4 outlines the numerical implementation of the coupled closure procedure used to determine the injection height.

An initial estimate of the injection height, h_i, is used to determine the shock separation location and corresponding primary flow properties. Using these quantities, the plateau pressure and flow turning characteristics are evaluated, allowing the plateau-region flow properties to be determined. The coupled mass and momentum conservation equations are then solved simultaneously for the updated injection height, h_{i+1}, and jet exit Mach number, $M_{j,e}$. These nonlinear conservation equations were solved simultaneously using the MATLAB® fzero root-finding routine. Specifically, the root, $M_{j,e}$, satisfies the following condition:

$$h_{mass} - h_{momentum} = 0 \tag{23}$$

https://doi.org/10.1017/aer.2026.10203 Published online by Cambridge University Press

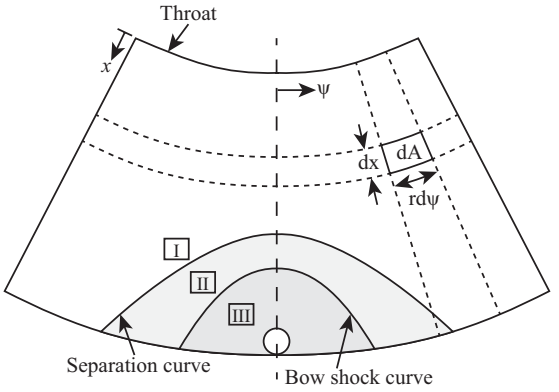


Figure 5. *Wall pressure distribution schematic in vicinity of secondary injection for conical nozzle.*

The procedure is repeated iteratively until the relative change in injection height between successive iterations satisfies

$$\frac{|h_{i+1} - h_i|}{h_i} < 0.01\%.$$

Following convergence, the final separation location is recomputed using the converged injection height.

3.3 Subroutine 2: force determination

The nozzle thrust is composed of the primary and secondary jet momentum contributions and the wall pressure contributions. The wall pressure distribution is divided into three distinct regions, as illustrated in Fig. 5: (I) undisturbed nozzle at P_{isen}, (II) separated region at P_{plat} and (III) elevated pressure region at P_{f}.

The thrust vector may be broken up into the axial and lateral components, denoted F_x and F_y, respectively. The x-component is parallel to the rocket axis, while the y-component is perpendicular. They are calculated according to Equations (24) and (25), respectively.

$$F_x = F_{x,\text{throat}} + F_{x,P} - P_{\text{amb}}A_{\text{e}} \tag{24}$$

$$F_y = F_{y,\text{jet}} + F_{y,P} \tag{25}$$

Here, $F_{x,\text{throat}}$ and $F_{y,\text{jet}}$ are the primary jet momentum at the nozzle throat, and the secondary jet momentum at the injector port, respectively. $F_{x,P}$ and $F_{y,P}$ represent the x- and y-components of the force due to the asymmetric wall pressure distribution, respectively. The primary jet momentum is calculated at the throat as shown in Equation (26):

$$F_{x,\text{throat}} = \dot{m}V_{\text{throat}} + P_{\text{throat}}A_{\text{throat}} \tag{26}$$

For a secondary jet injected perpendicular to the nozzle axis, the momentum contributions to the thrust are calculated according to Equation (27):

$$F_{y,\text{jet}} = \dot{m}_{\text{j}}V_{\text{j}} + \left(P_{\text{j}} - P_{\infty,x\text{IP}}\right)A_{\text{port}} \tag{27}$$

Here, P_{j} and $P_{\infty,x\text{IP}}$ are the pressure of the secondary jet at the injection port, and the pressure of the undisturbed primary flow at the injection port plane, respectively. Numerical integration of the pressure over the nozzle wall is performed to obtain the pressure contributions, $F_{x,P}$ and $F_{y,P}$.

https://doi.org/10.1017/aer.2026.10203 Published online by Cambridge University Press

3.3.1 Pressure contribution to the thrust vector

Given a continuous pressure distribution on an area, the force vector may be determined using Equation (28).

$$F_P = \int PndA \tag{28}$$

However, the pressure distribution over the nozzle wall is discretised into a grid of cells, each defined by indices m and n, corresponding to the x-axial and Ψ-angular positions, respectively. Numerical integration is performed over these discrete cells to approximate the total pressure contribution across the surface. In Equation (28), the unit outward normal, n, is defined by rotating the vector (0, 1, 0) by the nozzle half-angle, α_n, about the z-axis, and by ψ_n about the x-axis. Thus, the unit outward normal of each cell with index n is calculated using Equation (29):

$$n_n = \begin{bmatrix} 1 & 0 & 0 \\ 0 & \cos\psi_n & -\sin\psi_n \\ 0 & \sin\psi_n & \cos\psi_n \end{bmatrix} \begin{bmatrix} \cos\alpha_n & 0 & \sin\alpha_n \\ 0 & 1 & 0 \\ -\sin\alpha_n & 0 & \cos\alpha_n \end{bmatrix} \begin{bmatrix} 0 \\ 1 \\ 0 \end{bmatrix} \tag{29}$$

From Fig. 5, the cell area is calculated using the nozzle radius, r_m, according to Equation (30):

$$dS_m = r_m d\Psi dx \tag{30}$$

The force on each cell, indexed by (m, n) , is calculated using Equation (31):

$$dF_{P,mn} = P_m n_n r_m d\Psi dx \tag{31}$$

The overall force vector due to the wall pressure distribution, F_P, is calculated by summing over the nozzle length L for index m, and the full angular range of 360° for index n, as follows:

$$F_P = \sum_m \sum_n P_{mn} n_n r_m d\Psi dx \tag{32}$$

The pressure distribution on each (m, n)-indexed cell is elliptically interpolated between the undisturbed nozzle pressure and the pressure of each region (P_{plat} or P_f) as shown in Equation (33).

$$P_{mn} = P_{m,\text{isen}} + \left(P_{m,\text{isen}} - P_{\text{region}}\right)\sqrt{1 - \left(\frac{\psi_n r_m}{\psi_{m,\max} r_m}\right)^2} \tag{33}$$

Here, $\psi_{m,\max}$ describes the angular position of each region boundary, as described in the following section.

3.3.2 Region boundaries on the nozzle wall

The nozzle wall is separated into three distinct regions in order to define the pressure distribution as shown in Fig. 5. These regions are delineated by the bow shock curve and the separation curve, as illustrated in three dimensions in Fig. 6(a). The shock shape around a spherical obstruction was predicted to be hyperbolic by Billig [42].

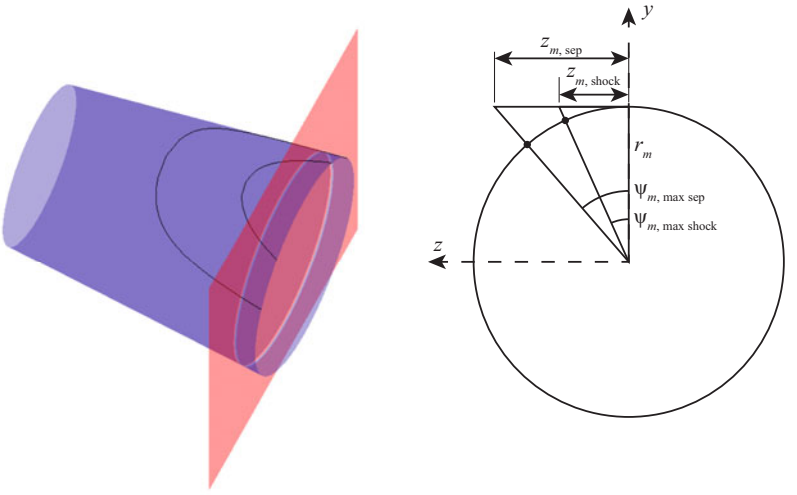
Building on this theory, Maarouf [17] proposed that the boundary layer separation profile is also hyperbolic. Using these theories, the shock and separation curves are assumed to have hyperbolic profiles that are asymptotic with the freestream Mach angle, θ. The Mach angle is evaluated using Equation (34) at the boundary layer separation position, x_s.

$$\sin\theta = \frac{1}{M_s} \tag{34}$$

A two-dimensional slice is shown in Fig. 6b to define $\psi_{\max}$ with respect to the z-coordinates of the shock and separation hyperbolas. At each x-position slice (indexed m), $\psi_{\max}$ is evaluated using Equation (35).

$$\tan\psi_{m,\max} = \frac{z_m}{r_m} \tag{35}$$

https://doi.org/10.1017/aer.2026.10203 Published online by Cambridge University Press



(a) (b)

Figure 6. *(a) Separation and shock hyperbolas on three-dimensional nozzle surface. (b) Schematic of* $\psi_{m,\max}$ *for two-dimensional slice of the nozzle at index m.*

Figure 7 illustrates the hyperbolic shock and separation profiles ahead of a spherical-nosed body with radius, h, based on Ref. (42). The x-coordinates of the centre of the injection port and focus point of the hyperbolas are x_{inj} and x_F, respectively. The shock standoff distance, Δ, and vertex radius of curvature, R_C, are also illustrated. The final shock and separation hyperbolas are presented in Equations (36) and (37), respectively:

$$\left[\frac{x-\left(x_{\text{inj}}-\Delta-R_C\cot^2\theta\right)}{R_C\cot^2\theta}\right]^2-\left[\frac{z_{\text{shock}}}{R_C\cot\theta}\right]^2=1 \tag{36}$$

$$\left[\frac{x-\left(x_c-R_s-R_s\cot^2\theta\right)}{R_s\cot^2\theta}\right]^2-\left[\frac{z_{\text{sep}}}{R_s\cot\theta}\right]^2=1 \tag{37}$$

Lastly, the radius of curvature for the separation curve, R_s, may be calculated from the focus point, x_F according to Equations (38) and (39).

$$x_F=x_{\text{inj}}-\Delta+R_C \tag{38}$$

$$R_s=x_F-x_s \tag{39}$$

The boundary layer separation position, x_s, was determined in subroutine 1.

3.3.3 Numerical implementation procedure for the thrust vector

Using the separation position from subroutine 1, the bow shock separation curves are computed, allowing the nozzle wall to be separated into three distinct pressure regions. The pressure distribution is calculated, and the pressure-driven force contribution is determined by integrating along the nozzle wall. The overall thrust vector is calculated by summing the pressure and jet momentum contributions. The procedure to solve for the thrust vector is schematically shown in Fig. 8.

https://doi.org/10.1017/aer.2026.10203 Published online by Cambridge University Press

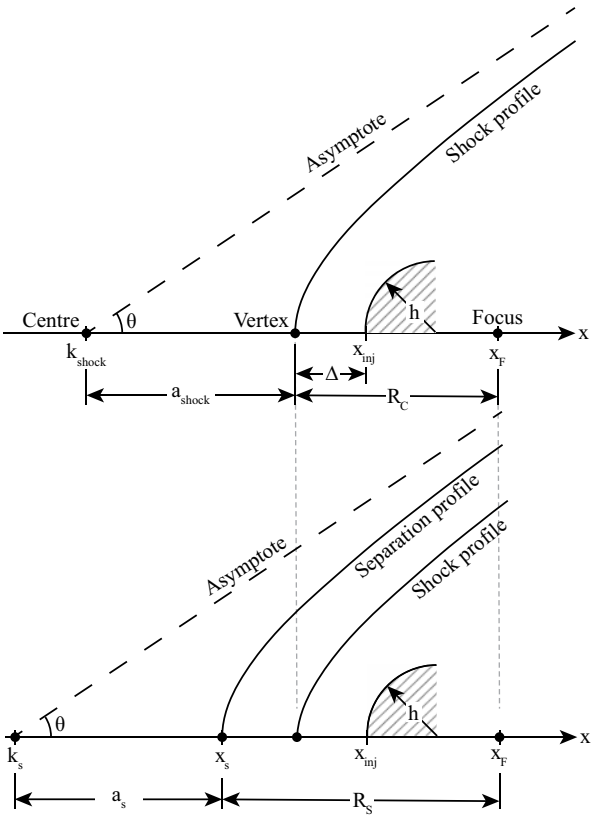


Figure 7. *Schematics of hyperbolic shock and separation profiles generated by a spherical-nosed body.*

4.0 Supporting CFD analysis

Three-dimensional CFD simulations were performed using OpenFOAM [43] with the pimpleCentralFOAM solver [44, 45] to examine dominant flow structures associated with secondary injection in supersonic nozzle flow. The simulations were intended to provide qualitative and semi-quantitative insight into separation behaviour, pressure development, and jet structure relevant to MMC-SIM assumptions, rather than to establish a standalone high-fidelity validation campaign.

A structured mesh with near-wall refinement was employed, and a three-level mesh refinement study was conducted to assess discretisation sensitivity. The medium mesh (5.2 m cells) was selected as a compromise between computational cost and solution variation. Additional details regarding mesh generation and boundary conditions, and verification are provided in Appendix A.

5.0 Problem setup

The geometry and flow properties were selected based on availability of three-dimensional SITVC experimental data in the literature, enabling validation of the model predictions. The simulation parameters, including nozzle geometry and flow conditions, were selected based on the experiments performed at the National Centre for Scientific Research Institute for Combustion, Aerothermics, Reactivity and Environment (ICARE) [19, 46–49], herein referred to as the University of Evry experiments. The experimental setup consisted of a blow-down supersonic wind tunnel supplying clean, oil-free, unheated air to both the primary and secondary jets through an SITVC conical nozzle, which exhausted into a vacuum

https://doi.org/10.1017/aer.2026.10203 Published online by Cambridge University Press

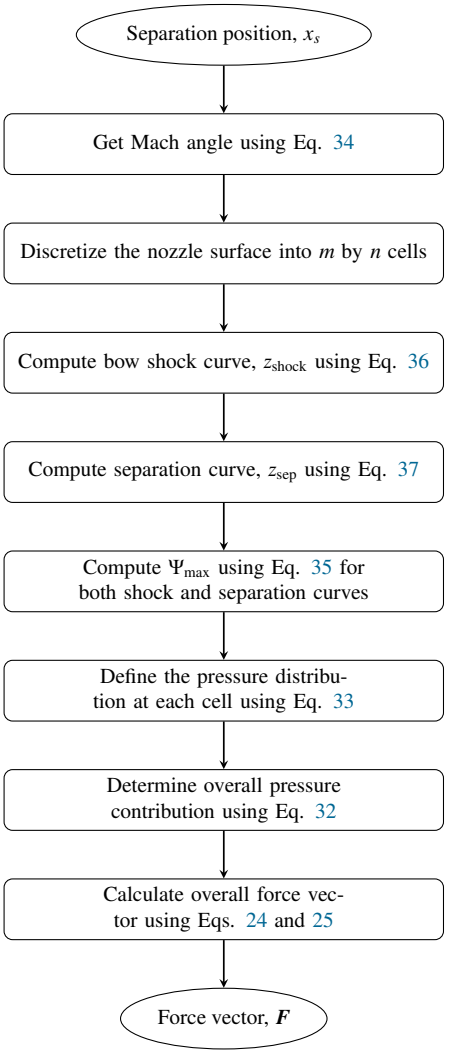


Figure 8. *Numerical implementation procedure for thrust vector computation.*

chamber. Experimental setup details are reported by the authors with some discrepancies between the various papers [19, 20, 37, 49]. The nozzle geometry and stagnation temperature were matched to the latest paper [20]. The experimental data used for comparison with the results in this work are from the earlier three papers [19, 37, 49], as the latest paper does not report the data required. The conical nozzle geometry used is presented in Table 1. This geometry yields a half-angle and area ratio of approximately 5.87° and 4.234, respectively. Given the potential inconsistencies between the simulation inputs and the experimental setup, errors are expected to arise.

The centre of the injection port is located at 90% of the nozzle length ($x_{inj} = 90.0$ mm). Note that the origin of the x-coordinate is set at the nozzle throat. The injection is perpendicular to the primary rocket axis, not the conical nozzle wall. Both primary and secondary flows are air (with a molar mass of 28.96 kg/kmol) at a stagnation pressure of 260 K and an inlet Mach of 1. The primary flow has a stagnation pressure of 300 kPa.

The secondary jet stagnation pressure is varied to evaluate its effect on TVC performance. The secondary pressure ratio (SPR) is defined in Equation (40) as the stagnation pressure ratio of the secondary

https://doi.org/10.1017/aer.2026.10203 Published online by Cambridge University Press

Table 1. *Conical nozzle geometry*

Dimension	Value (mm)
Throat radius	9.72
Exit radius	20.0
Nozzle length	100.0
Injector port position	90.0
Injector port diameter	6.15

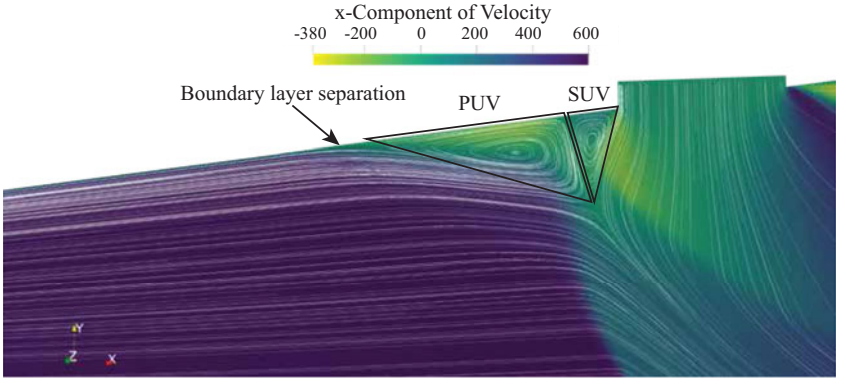


Figure 9. *Streamlines of two opposing vortices upstream of injector.*

to the primary jets. Analytical and numerical simulations are performed at SPR values of 0.667, 0.833, 1 and 1.167.

$$\mathrm{SPR} = \frac{P_{\mathrm{tj}}}{P_{\mathrm{t}}} \tag{40}$$

The SITVC nozzle exhausts into a vacuum chamber with air at an ambient temperature and pressure of 290 K and 8 kPa, respectively.

6.0 Results

This section first presents supporting CFD analysis used to examine dominant SITVC flow structures and assess assumptions underlying MMC-SIM. Experimental comparisons are then used to evaluate predictive performance of the analytical framework.

6.1 Overview of the interaction field

A qualitative analysis of the CFD simulations offers significant insights into the flow features within an SITVC nozzle. Figure 9 presents the streamlines of the flow near the secondary injection port.

Upstream of the secondary gas injection, boundary layer separation occurs, creating two distinct counter-rotating vortices in the plateau region. The primary upstream vortex (PUV), which rotates counter-clockwise, occupies the larger portion of the separation zone, while the secondary upstream vortex (SUV) rotates clockwise.

The primary nozzle flow accelerates in the undisturbed region as expected. At the secondary injection port, the jet is introduced sonically, rapidly expanding and accelerating into the primary flow. The Mach number distribution in Fig. 10 provides a detailed view of the regions directly around the injection port. Here, the plateau flow is subsonic upstream of the injection site, a result of the secondary jet obstructing

https://doi.org/10.1017/aer.2026.10203 Published online by Cambridge University Press

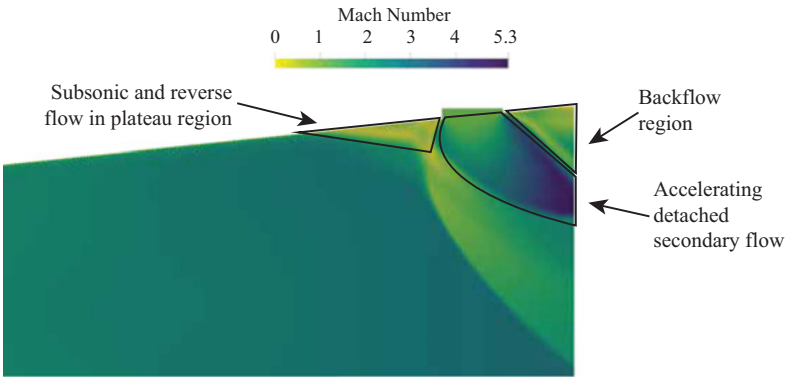


Figure 10. *Distribution of the Mach number in an SITVC nozzle in the injector port region.*

and deflecting the primary nozzle flow. This deflection occurs via two main mechanisms: an oblique separation shock generated upstream of the injection point, and a bow shock surrounding the jet.

Downstream of the injection, a distinct subsonic region forms, marked by some degree of backflow. This region is associated with extremely low static pressures, lower than the ambient back pressure, creating conditions that allow external flow to re-enter the nozzle. This low-pressure zone, strongly influenced by the stagnation pressure of the external atmosphere, is detrimental to thrust vectoring performance. By driving backflow into the nozzle, it counteracts the desired redirection of thrust, and minimising this low-pressure region is crucial for improving overall vectoring efficiency.

The secondary jet does not reattach to the nozzle wall following injection. Instead, the flow remains detached, suggesting that the jet expansion and interactions with the primary flow prevent reattachment under the current conditions. This detachment impacts the effective direction and magnitude of the thrust vector, highlighting areas for potential improvement in future SITVC nozzle designs aimed at optimising reattachment and minimising backflow zones for enhanced control authority.

This observation also reveals a limitation in MMC-SIM and similar blunt-body models, which assume the secondary gas deflects parallel to the nozzle wall. However, CFD analysis shows that the jet may remain partially detached under certain conditions. Future work could refine the control volume by incorporating a more accurate representation of the equivalent obstruction, based on this detached flow pattern.

6.2 Secondary jet shape

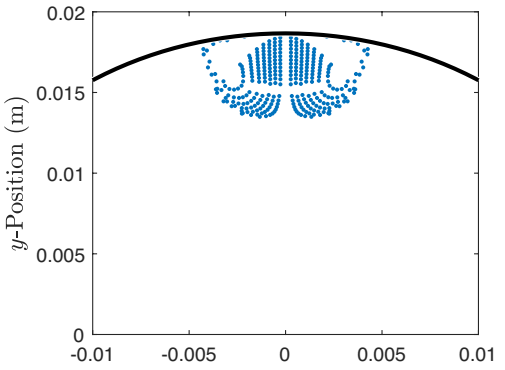
Figure 11 presents cross-sections of traced secondary jet streamlines taken at various x-positions along the nozzle. Observations reveal that the jet continues to expand at least to the exit face of the nozzle. Additionally, each cross-section has non-uniform pressure and density distributions. The cross-sectional shape of the jet is difficult to pinpoint, but more closely approximates an elliptical area than a semi-circular one.

These observations reinforce the difficulty of prescribing downstream jet geometry or exit conditions a priori, as is commonly required in existing blunt-body formulations. MMC-SIM avoids this dependence by determining the effective obstruction height through coupled conservation constraints rather than through assumed downstream jet structure.

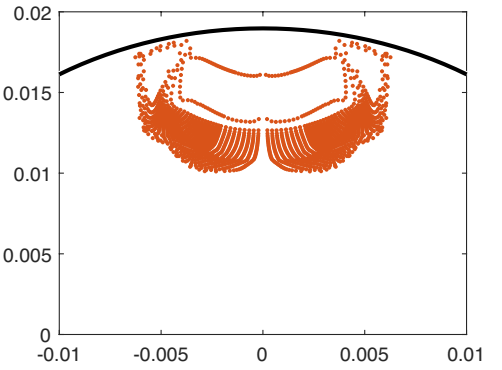
6.3 Boundary layer separation

To compare the boundary layer separation positions from MMC-SIM predictions and CFD simulations, the boundary layer separation position is defined as the location of zero wall shear stress ($\tau_w = 0$). For

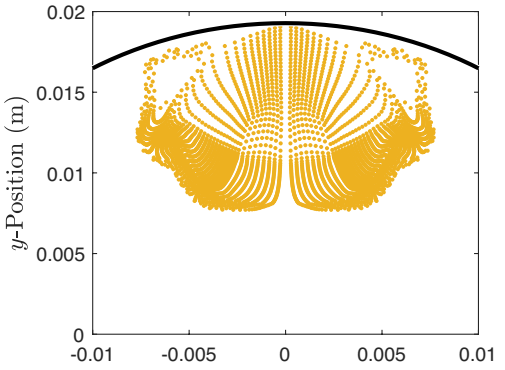
https://doi.org/10.1017/aer.2026.10203 Published online by Cambridge University Press



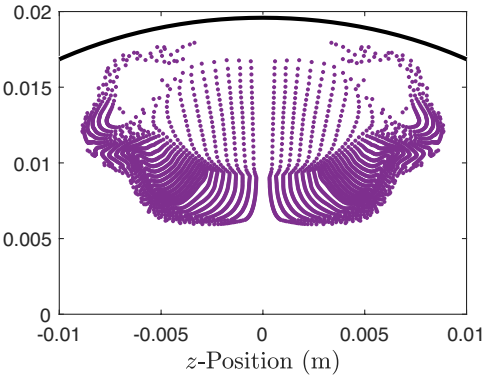
(a) x = 87 mm



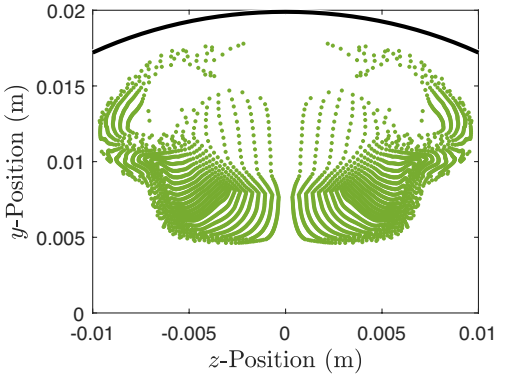
(b) x = 90 mm



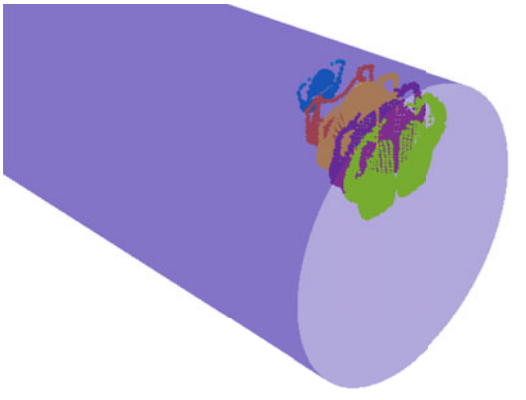
(c) x = 93 mm



(d) x = 96 mm



(e) x = 99 mm



(f) Slices in 3D nozzle.

Figure 11. *(a)–(e) Cross-sections of secondary jet streamlines with corresponding nozzle wall at various x-positions. (f) Cross-sections within the three-dimensional nozzle.*

https://doi.org/10.1017/aer.2026.10203 Published online by Cambridge University Press

Table 2. *Comparison of separation standoff distance results*

	X_s (mm)		
SPR	MMC-SIM	CFD	% Error
0.667	15.29	12.9	18.5%
0.833	15.89	13.6	16.9%
1.000	16.46	14.5	13.5%
1.167	16.98	15.4	10.2%

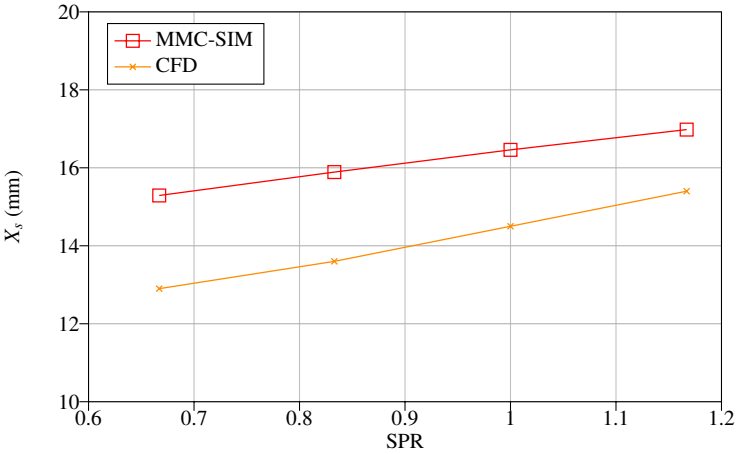


Figure 12. *Comparison of separation distance as a function of SPR between MMC-SIM analyses and CFD results.*

the case of SPR = 1.000, the CFD simulation results indicate that separation occurs at an x-position of 75.5 mm. Using Equation (1) results in a separation standoff distance of $X_s = 14.5$ mm. The CFD-derived separation location indicates that MMC-SIM captures the correct upstream separation trend and order of magnitude, despite the simplified equivalent-obstruction representation. Compared to the MMC-SIM prediction of 16.46 mm, this yields a 13.5% error. Table 2 summarises separation standoff distances across various SPR values, with an average error of 14.8% when compared to CFD results. Additionally, Fig. 12 compares the separation standoff distances between MMC-SIM analyses and CFD results.

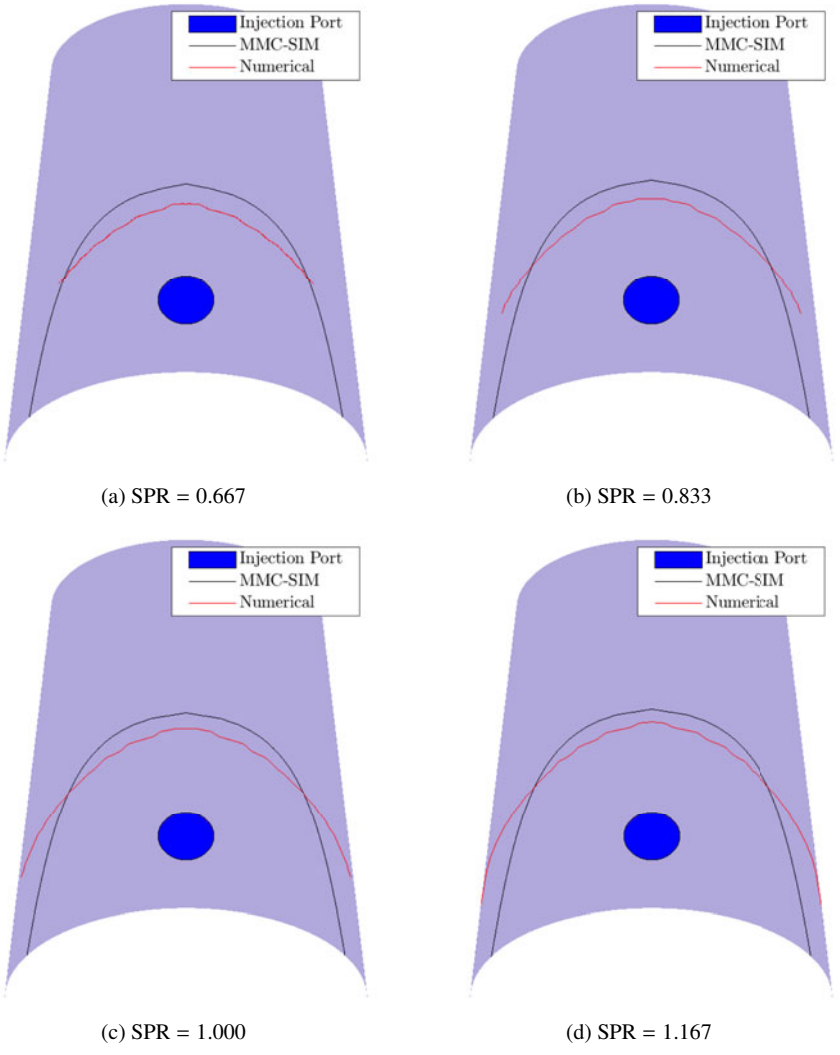
Furthermore, the separation position predicted by the Evry model for the SPR = 1 case was provided by Dr. Sellam (personal communication, October 20, 2023) as 84 mm. This yields a separation distance of 6 mm – considerably shorter than that predicted by CFD.

Qualitative comparisons between the analytically and numerically determined separation curves are illustrated in Fig. 13. The CFD-derived separation curves show localised fluctuations near the separation boundary but preserve the overall topology and upstream trend.

Overall, the MMC-SIM code over-predicts the separation distance, with the predicted separation point occurring further upstream than observed in CFD simulations. Additionally, the shape of the separation curve generated by the MMC-SIM code follows a narrower, hyperbolic profile, compared to the broader curve produced by the CFD results. Such differences highlight a potential area for refinement of the MMC-SIM code, particularly in better representing the separation curve's profile to improve the accuracy of thrust vector predictions.

These comparisons are intended to assess whether MMC-SIM captures the dominant separation behaviour associated with SITVC interactions, rather than to establish exact correspondence with the CFD solution.

https://doi.org/10.1017/aer.2026.10203 Published online by Cambridge University Press



(a) SPR = 0.667 (b) SPR = 0.833

(c) SPR = 1.000 (d) SPR = 1.167

Figure 13. *Comparison between boundary layer separation curves determined by MMC-SIM and CFD simulations on nozzle wall.*

6.4 Pressure profile

The CFD-derived pressure profile along the wall at 0°, illustrated in Fig. 14, provides insight into the pressure contribution represented within MMC-SIM. As is typical of expanding nozzle flows, the pressure decreases as the flow progresses. Around 72 mm, the adverse pressure gradient begins to develop, as indicated by a reversal in the pressure trend. At some point, the adverse pressure triggers boundary layer separation. The pressure reaches its first peak in the plateau region with a maximum value of 30.9 kPa. Ahead of the secondary injection port, there is a noticeable second pressure spike, reaching 51.5 kPa, as the flow encounters the bow shock. Beyond this, the pressure sharply increases, reaching the secondary jet inlet pressure, before sharply decreasing. The pressure drop downstream of the obstruction indicates the presence of localised backflow created by ambient air entering the nozzle.

Figure 15 further illustrates how the pressure along the nozzle wall evolves with increasing angular position, Ψ. The plot reveals an attenuated effect, where the influence of the secondary jet diminishes with increasing distance from the injection point.

https://doi.org/10.1017/aer.2026.10203 Published online by Cambridge University Press

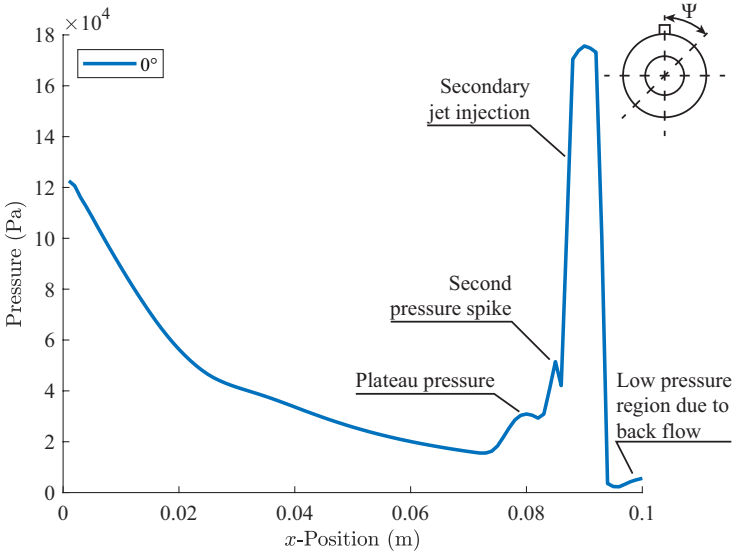


Figure 14. *Numerically generated wall pressure distribution for SITVC nozzle operating with SPR = 1 for* $\Psi = 0°$.

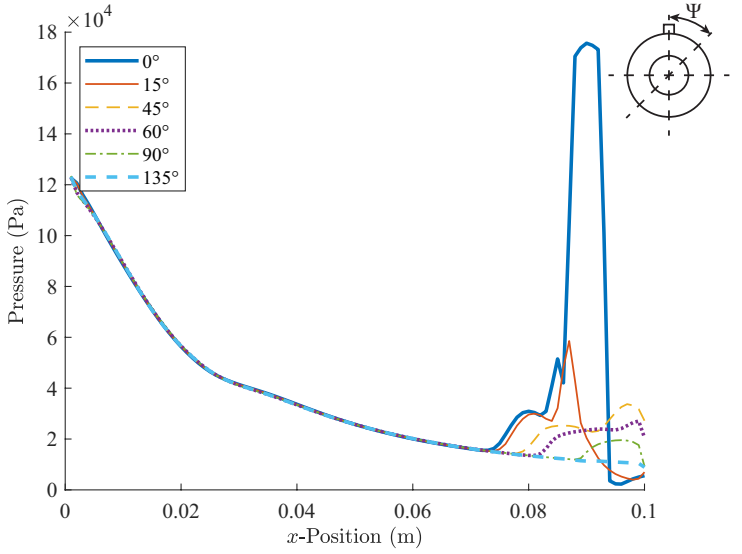


Figure 15. *Numerically generated wall pressure distribution for SITVC nozzle operating with SPR = 1 for various angles,* Ψ.

Next, the pressure profiles generated using CFD simulations and MMC-SIM are compared for various angles, as illustrated in Fig. 16. Both profiles exhibit a similar trend, showing an initial pressure decrease, followed by an increase ahead of the obstruction. This is consistent with flow behaviour in a supersonic nozzle with a lateral jet injection. While the magnitudes are similar, the numerically obtained pressure profile is systematically higher than that of the analytical model in the undisturbed region. The pressure profiles for other SPR values behave similarly. Overall, MMC-SIM reproduces the dominant pressure-rise and separation trends observed in the CFD results.

https://doi.org/10.1017/aer.2026.10203 Published online by Cambridge University Press

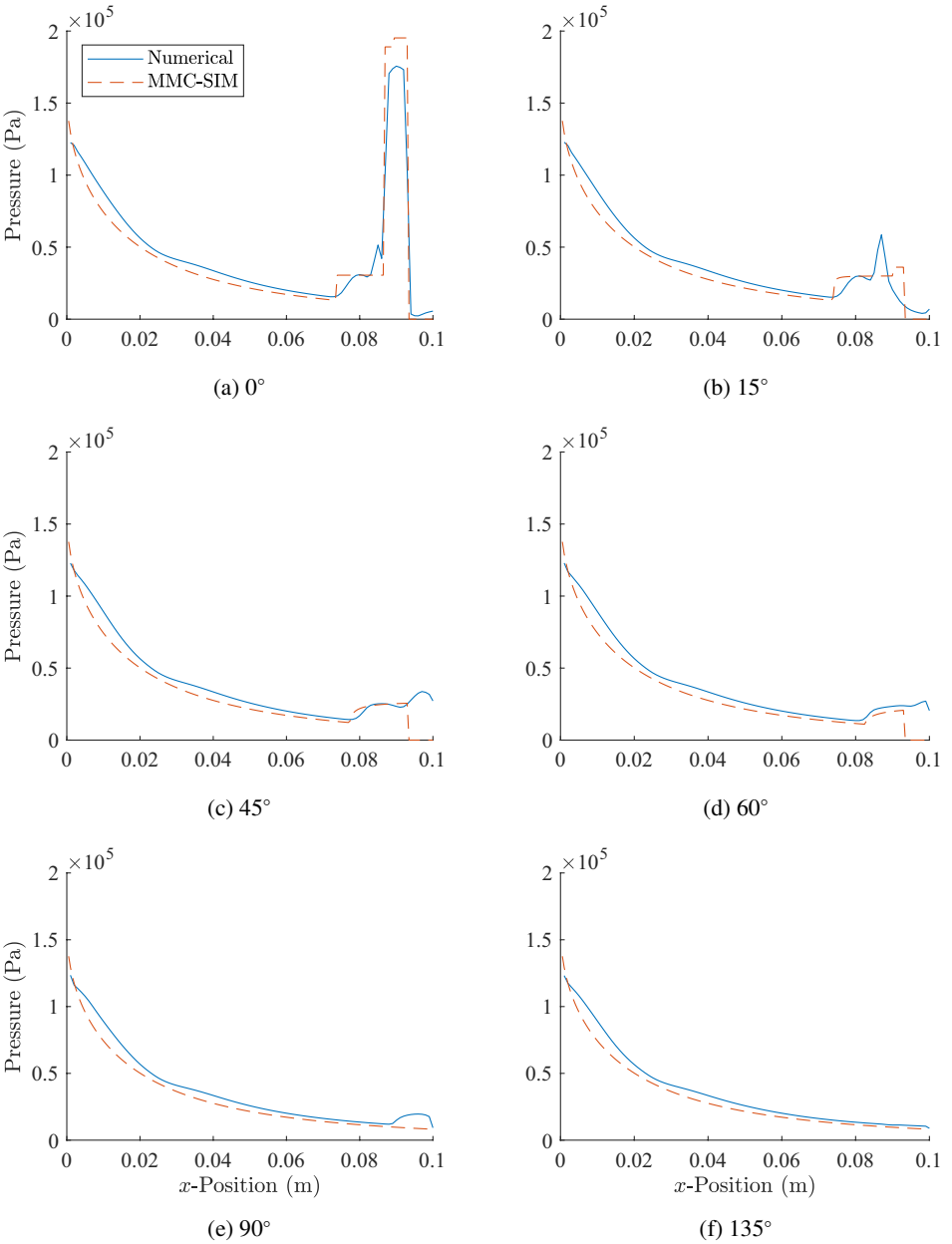


Figure 16. *Comparison of CFD and analytical wall pressure distributions at various angles for SPR = 1.*

6.5 Thrust vectoring

The primary validation of MMC-SIM is performed through comparison with experimentally measured thrust vector data from the University of Evry SITVC experiments. Particular emphasis is placed on assessing whether the coupled mass-momentum closure improves the prediction of pressure-driven lateral force while retaining the computational simplicity of reduced-order blunt-body modelling in Fig. 17.

The thrust vector predictions produced by MMC-SIM are analysed as a function of SPR. Tables 3 and 4 compare the thrust vector results generated by MMC-SIM with experimental measurements,

https://doi.org/10.1017/aer.2026.10203 Published online by Cambridge University Press

Table 3. *Validation of MMC-SIM thrust vector with experimental data [19]*

	F_y (N)			F_x (N)		
SPR	Exp	MMC-SIM	% Error	Exp	MMC-SIM	% Error
0.667	12.4	12.85	3.7%	126.8	129.78	2.4%
0.833	15.0	15.21	1.4%	128.3	129.84	1.2%
1.000	18.4	17.52	4.8%	127.8	129.89	1.6%
1.167	20.5	19.82	3.3%	127.3	129.93	2.1%

Table 4. *Validation of MMC-SIM thrust vector angles with experimental data [19]*

	Thrust Vector Angle (°)		
SPR	Exp	MMC-SIM	% Error
0.667	5.59	5.66	1.3%
0.833	6.67	6.68	0.2%
1.000	8.19	7.68	6.2%
1.167	9.15	8.67	5.2%

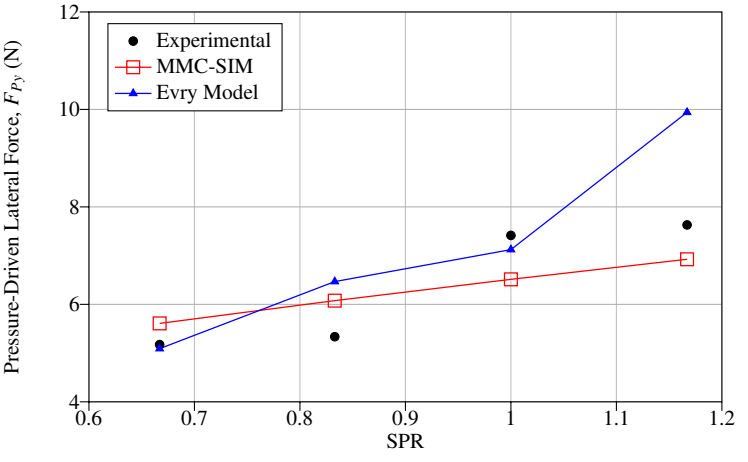


Figure 17. *Pressure contribution to lateral force compared to SPR derived from the MMC-SIM code and the Evry model and experiments [19].*

accompanied by calculated percent errors. MMC-SIM yields average errors of 3.3% in predicting total lateral thrust, and 3.2% in estimating the thrust vector deflection angle.

In the University of Evry's experiments, the axial and lateral thrust were directly measured using force transducers [19]. By subtracting the secondary jet momentum, F_{jy}, from the measured lateral thrust, the remaining component approximates the pressure-driven force. Note that the viscous forces are considered negligible, as CFD simulations show that they are approximately one order-of-magnitude smaller than pressure forces [36].

Table 5 compares the results of the MMC-SIM code and the Evry model (the current state-of-the-art from the University of Evry) with experimental data reported by the same research group [19]. MMC-SIM achieves an average error of 8.3% and a maximum error of 11.8% in predicting the pressure-driven lateral thrust. Furthermore, it offers a 2.5-fold improvement in accuracy over the Evry model's maximum error of 30.7%.

It should be noted that reduced-order models for thrust vectoring inherently rely on semi-empirical relations for interactions in the separation region ahead of the injection. In the MMC-SIM formulation,

https://doi.org/10.1017/aer.2026.10203 Published online by Cambridge University Press

Table 5. *Comparison of the pressure-driven lateral force between the MMC-SIM code and Evry model results with experimental data [19]*

		Evry model		MMC-SIM	
SPR	Experimental	Value	% Error	Value	% Error
0.667	5.154	5.091	1.2%	5.609	8.8%
0.833	5.871	6.467	10.2%	6.076	3.5%
1.000	7.388	7.123	3.6%	6.513	11.8%
1.167	7.605	9.940	30.7%	6.925	8.9%

these effects are captured through well-established empirical relations, which are selected based on prior validated models and physical consistency. While this introduces residual uncertainty, particularly in lateral force prediction due to sensitivity to separation distance, the core advantage of the present approach lies in enforcing global conservation constraints and reducing dependence on exit-flow assumptions, thereby improving overall consistency across force components and vector angle predictions.

7.0 Conclusion

A central limitation of existing blunt-body SITVC models is that closure of the effective obstruction problem typically relies on prescribed downstream jet conditions or auxiliary assumptions regarding jet behaviour. These assumptions reduce reproducibility and can introduce inconsistencies with conservation principles.

MMC-SIM addresses this limitation by determining the effective obstruction geometry through simultaneous enforcement of mass and momentum conservation. This coupled closure eliminates the need to prescribe downstream jet conditions a priori, yielding a transparent and fully specified reduced-order modelling framework. Validation against cold-gas experiments demonstrates strong agreement, yielding average and maximum lateral force errors of just 3.3% and 4.8%, respectively. Notably, MMC-SIM reduces the error in the pressure-driven lateral force by up to 2.5 times compared to current prominent models in the field.

Supporting CFD analysis demonstrated that MMC-SIM captures several dominant SITVC flow features, including upstream separation behaviour and asymmetric wall pressure development, while also identifying limitations associated with the simplified equivalent-obstruction representation.

The resulting framework provides a physically constrained, reproducible and computationally efficient tool for thrust vector prediction suitable for preliminary nozzle design, parametric analysis and integration into reduced-order flight simulation environments.

Acknowledgments. Funding for this work was provided by Dr. Craig Johansen's Discovery Grant from the Natural Sciences and Engineering Research Council (NSERC) of Canada.

Competing interests. The authors declare that they have no known competing financial interests or personal relationships that could have appeared to influence the work reported in this paper.

References

[1] Messinger, T., Hill, C., Quinn, D., Stannard, D., Doerksen, G. and Johansen, C.T. Development and test flight of the Atlantis I nitrous oxide/paraffin-based hybrid rocket, AIAA Propulsion and Energy 2019 Forum, Indianapolis, IN. American Institute of Aeronautics and Astronautics, 2019.

[2] Schmierer, C., Kobald, M., Tomilin, K., Fischer, U. and Schlechtriem, S. Low cost small-satellite access to space using hybrid rocket propulsion, *Acta Astronaut.*, 2019, **159**, pp 578–583.

[3] Sutton, G.P. and Biblarz, O. *Rocket Propulsion Elements*, 9th edition, Wiley, 2017, Hoboken, NJ, USA.

[4] Pelouch, J. Final report thrust vector control system study program. Technical report, NASA, 1970.

[5] Green, C.J. and McCullough, F. Liquid injection thrust vector control. Technical report, 1961.

https://doi.org/10.1017/aer.2026.10203 Published online by Cambridge University Press

[6] Newton, J. Secondary injection for thrust vector control, Research Summary No 36-9, 1, NASA Jet Propulsion Laboratory, 1961, Pasedena, CA, USA.
[7] Hozaki, S., Gagnon, R., Mayer, E., Tromblay, J. and Wu, J. Investigation of boundary layer parameters in APG nozzle and the flow interference caused by secondary injection. NASA-CR-50606, National Engineering Science Co., Pasadena, CA, USA, 1963.
[8] Carroll, K.A., Cherrington, W., Greatrix, D., Harry, C., Lapp, P., Porcher, J., Sokoloff, A. Spencer, H., Trumpour, A. and Viechweg, M. Microsatellite launch system technical feasibility study project final report. Technical report, Continuum Aerospace, 2009.
[9] Zmijanovic, V., Leger, L., Sellam, M. and Chpoun, A. Assessment of transition regimes in a dual-bell nozzle and possibility of active fluidic control, *Aerosp. Sci. Technol.*, 2018, **82–83**, pp 1–8.
[10] Broadwell, J.E. Analysis of the fluid mechanics of secondary injection for thrust vector control, *AIAA J.*, 1963, **1**, (5), pp 1067–1075.
[11] Karamcheti, K. and Tao-Sze Hsia, H. Integral approach to an approximate analysis of thrust vector control by secondary injection, *AIAA J.*, 1963, **1**, (11), pp 2538–2544.
[12] Spaid, F.W. A study of secondary injection of gases into a supersonic flow. PhD thesis, California Institute of Technology, Pasadena, California, 1964.
[13] Walker, R.E., Stone, A.R. and Shandor, M. Secondary gas injection in a conical rocket nozzle i. effect of orifice diameter and molecular weight of injectant. Technical report, The Johns Hopkins University Applied Physics Laboratory, 1962.
[14] Wilson, W.G. and Comparin, R.A. Analytical investigation of side jet supersonic stream interaction including vortex flow in rocket nozzles for thrust vector control. Technical Report NASA CR 66754, Virginia Polytechnic Institute, Blacksburg, Virginia, 1969.
[15] Wu, J.-M., Chapkis, R.L. and Mager, A. Approximate analysis of thrust vector control by fluid injection, *ARS J.*, 1961, **31**, (12), pp 1677–1685.
[16] Zukoski, E.E. and Spaid, F.W. Secondary injection of gases into a supersonic flow, *AIAA J.*, 1964, **2**, (10), pp 1689–1696.
[17] Maarouf, N. Modélisation des phénomènes dissymétriques dans le divergent des tuyères supersoniques propulsives: Application a la vectorisation de la poussée. PhD thesis, L'Université D'Évry-Val D'Essonne, 2008.
[18] Mangin, B. Vectorisation fluidique de la poussée d'une tuyère plane supersonique. PhD thesis, Université d'Orléans, 2006.
[19] Sellam, M., Chpoun, A., Zmijanovic, V. and Lago, V. Fluidic thrust vectoring of an axisymmetrical nozzle: an analytical model, *Int. J. Aerodyn.*, 2012, **2**, (2/3/4), p 193.
[20] Zmijanovic, V., Leger, L., Depussay, E., Sellam, M. and Chpoun, A. Experimental-numerical parametric investigation of a rocket nozzle secondary injection thrust vectoring, *J. Propul. Power*, 2016, **32**, (1), pp 196–213.
[21] Balu, R., Marathe, A.G., Paul, P.J. and Mukunda, H.S. Analysis of performance of a hot gas injection thrust vector control system, *J. Propul. Power*, 1991, **7**, (4), pp 580–585.
[22] Huang, W. Transverse jet in supersonic crossflows, *Aerosp. Sci. Technol.*, 2016, **50**, pp 183–195.
[23] Zhang, Z., McCreton, S.F., Awasthi, M., Wills, A.O., Moreau, D.J. and Doolan, C.J. The flow features of transverse jets in supersonic crossflow, *Aerosp. Sci. Technol.*, 2021, **118**, pp 107058.
[24] Chen, J.-L. and Liao, Y.-H. Parametric study on thrust vectoring with a secondary injection in a convergent-divergent nozzle, *J. Aerosp. Eng.*, 2020, **33**, (4), pp 04020020.
[25] Chen, X., Fang, W., Liu, Z., Wu, K., Li, H., Sethuraman, V.R.P., Kumar, S.A. and Li, K. Three-dimensional internal flow characteristics of bypass shock-induced thrust vector control, *Aerosp. Sci. Technol.*, 2026, **168**, pp 111015.
[26] Chouicha, R., Sellam, M. and Bergheul, S. Effect of chemical reactions on the fluidic thrust vectoring of an axisymmetric nozzle, *Int. J. Aviat. Aeronaut. Aerosp.*, 2019, **6**, (5), article 16.
[27] Lee, E., Kang, H. and Kwon, S. Demonstration of thrust vector control by hydrogen peroxide injection in hybrid rockets, *J. Propul. Power*, 2019, **35**, (1), pp 109–114.
[28] Sharjad, A., Bijo, B. and Ranjith, S.K. Numerical investigation on secondary injection and thrust vector control in a planar double divergent nozzle, *Prog. Eng. Sci.*, 2024, **1**, (4), pp 100017.
[29] Wu, K., Jin, Y. and Kim, H.D. Hysteretic behaviors in counter-flow thrust vector control, *J. Aerosp. Eng.*, 2019, **32**, (4), pp 04019041.
[30] Wu, K., Kim, T.H. and Kim, H.D. Theoretical and numerical analyses of aerodynamic characteristics on shock vector control, *J. Aerosp. Eng.*, 2020, **33**, (5), pp 04020050.
[31] Younes, K., Grenke, A., Hickey, J.-P., Gagnon, M. and Elzein, B. Enhanced delayed detached eddy simulations of shock-vector control, 23rd AIAA International Space Planes and Hypersonic Systems and Technologies Conference, Montreal, Quebec, Canada. American Institute of Aeronautics and Astronautics, 2020.
[32] Deng, R., Kong, F. and Kim, H.D. Numerical simulation of fluidic thrust vectoring in an axisymmetric supersonic nozzle, *J. Mech. Sci. Technol.*, 2014, **28**, (12), pp 4979–4987.
[33] Younes, K. and Hickey, J.-P. Fluidic thrust shock-vectoring control: a sensitivity analysis. *AIAA J.*, 2020, **58**, (4), pp 1887–1890.
[34] Spaid, F.W. and Zukoski, E.E. A study of the interaction of gaseous jets from transverse slots with supersonic external flows, *AIAA J.*, 1968, **6**, (2), pp 205–212.
[35] Zukoski, E.E. Turbulent boundary-layer separation in front of a forward-facing step, *AIAA J.*, 1967, **5**, (10), pp 1746–1753.
[36] Abdelwahab, N. Mass- and momentum-conserved secondary injection model (MMC-SIM) for thrust vector control analysis. Master's thesis, University of Calgary, 2024.

https://doi.org/10.1017/aer.2026.10203 Published online by Cambridge University Press

[37] Zmijanovic, V., Lago, V., Leger, L., Depussay, E., Sellam, M. and Chpoun, A. Thrust vectoring effects of a transverse gas injection into a supersonic cross flow of an axisymmetric convergent-divergent nozzle, Progress in Propulsion Physics, St. Petersburg, Russian. EDP Sciences, 2013, pp 227–256.
[38] John, J.E. and Keith, T.G. *Gas dynamics*, 3rd edition. Pearson, 2006, Toledo, Ohio.
[39] Rowlands, A. *Physics of Digital Photography*, IOP Publishing, 2017, Bristol, UK.
[40] Lees, L. Hypersonic flow. *J. Spacecr. Rockets*, 2003, **40**, (5), pp 700–735.
[41] Anderson, J.D. Jr. *Hypersonic and High Temperature Gas Dynamics*. American Institute of Aeronautics and Astronautics, 2nd edition, 2006, Reston, VA, USA.
[42] Billig, F.S. Shock-wave shapes around spherical-and cylindrical-nosed bodies, *J. Spacecr. Rockets*, 1967, **4**, (6), pp 822–823.
[43] Weller, H.G., Tabor, G., Jasak, H. and Fureby, C. A tensorial approach to computational continuum mechanics using object-oriented techniques, *Comput. Phys.*, 1998, **12**, (6), pp 620–631.
[44] Kraposhin, M., Bovtrikova, A. and Strijhak, S. Adaptation of Kurganov-Tadmor numerical scheme for applying in combination with the PISO method in numerical simulation of flows in a wide range of Mach numbers, *Procedia Comput. Sci.*, 2015, **66**, pp 43–52.
[45] Kraposhin, M.V., Banholzer, M., Pfitzner, M. and Marchevsky, I.K. A hybrid pressure-based solver for nonideal single-phase fluid flows at all speeds. *Int. J. Numer. Methods Fluids*, 2018, **88**, (2), pp 79–99.
[46] Chpoun, A., Sellam, M., Zmijanovic, V. and Leger, L. Secondary injectant gas thermodynamic properties effects on fluidic thrust vectoring performances of a supersonic nozzle. *30th International Symposium on Shock Waves 1*. 2017, vol. 1, pp 539–543.
[47] Sellam, M., Zmijanovic, V., Leger, L. and Chpoun, A. Assessment of gas thermodynamic characteristics on fluidic thrust vectoring performance: analytical, experimental and numerical study, *Int. J. Heat Fluid Flow*, 2015, **53**, pp 156–166.
[48] Zmijanovic, V. Secondary injection fluidic thrust vectoring of an axisymmetric supersonic nozzle. PhD thesis, 2013.
[49] Zmijanovic, V., Lago, V., Sellam, M. and Chpoun, A. Thrust shock vector control of an axisymmetric conical supersonic nozzle via secondary transverse gas injection, *Shock Waves*, 2014, **24**, (1), pp 97–111.
[50] Menter, F.R., Kuntz, M. and Langtry, R. Ten years of industrial experience with the SST turbulence model. *Heat Mass Transf.*, 2003, **4**, (1), pp 625–632.

APPENDIX

8.0 Numerical methodology

8.1 Mesh generation and boundary conditions

As noted in Section 4, the standard OpenFOAM/pimpleCentralFOAM solver for 3D turbulent high-speed flows was applied, using the k-ω shear stress transport (SST) [50] turbulence model and a 5.3 m cell mesh. The computational domain and boundary conditions are indicated in Fig. A1.

Primary and secondary sonic inlets were defined using stagnation properties for temperature and pressure, providing a fixed value for velocity. No-slip, adiabatic conditions were applied on the primary nozzle wall, while slip, adiabatic conditions were adopted for the secondary nozzle wall. The far

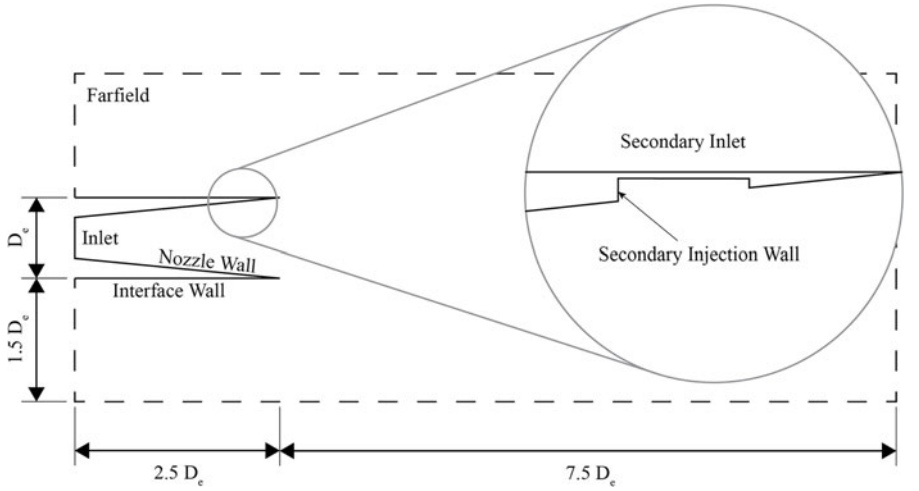


Figure A1. *Schematic of boundary conditions and domain.*

https://doi.org/10.1017/aer.2026.10203 Published online by Cambridge University Press

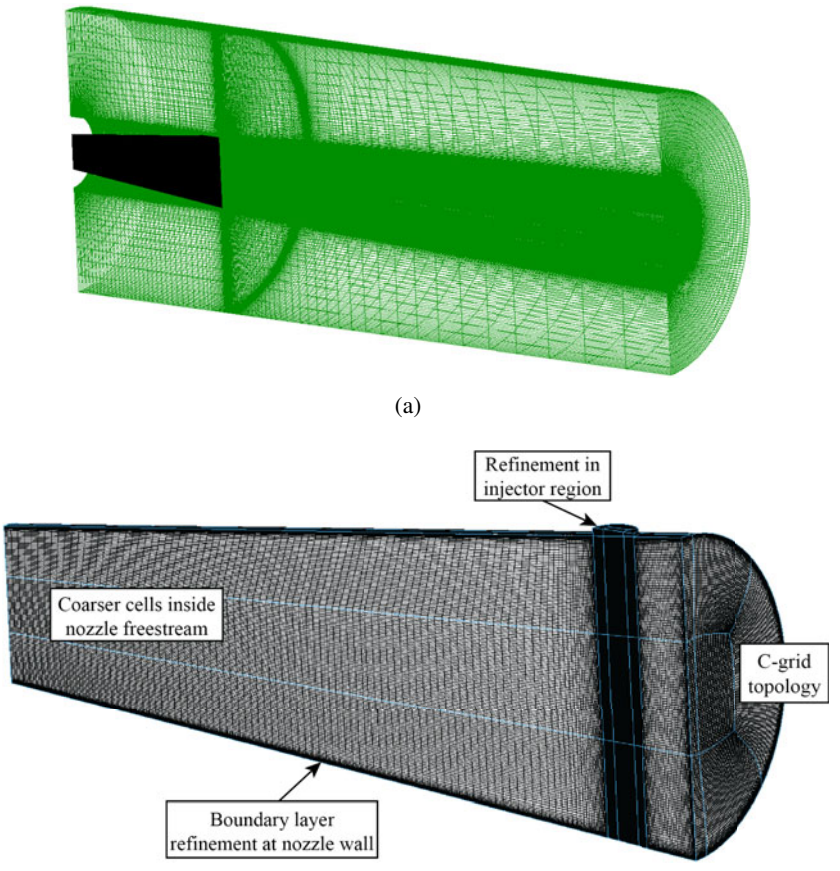


Figure A2. *(a) Overview of the medium refinement computational mesh with the farfield in green. (b) Fully structured mesh of axisymmetric nozzle with secondary injection.*

field was treated as an inlet-outlet boundary to account for possible vortices exiting the domain; only half the conical nozzle was simulated by applying symmetry boundary conditions on a vertical centre plane through the nozzle centreline. Far-field domain sizing was chosen to minimise boundary condition effects and allow capture of flow development outside the nozzle for both over- and under-expanded conditions, while minimising computational requirements. A 3D structured mesh was developed using intersecting C-grid topologies for both the primary nozzle and the secondary injection port. An overview of the mesh is provided in Fig. A2(a), with Fig. A2(b) illustrating the extra refinement included to resolve secondary port injected flow. Near-wall mesh refinement was undertaken to ensure accurate resolution of wall boundary layers (resulting in typical values of non-dimensional wall distance, y^+, were $\mathcal{O}$ (1)).

Cite this article: Abdelwahab N. and Johansen C. (2026). Mass- and momentum-conserved secondary injection model (MMC-SIM) for thrust vector control analysis. *The Aeronautical Journal*, **130**, 3054–3080. https://doi.org/10.1017/aer.2026.10203

https://doi.org/10.1017/aer.2026.10203 Published online by Cambridge University Press